Applied Ocean Research 105 (2020) 102368

Contents lists available at ScienceDirect

Applied Ocean Research

journal homepage: www.elsevier.com/locate/apor

Model uncertainty assessment for wave- and current-induced global response of a curved floating pontoon bridge

Thomas Viuff[a,b,*], Xu Xiang[c], Ole Øiseth[d], Bernt Johan Leira[a]

[a] Department of Marine Technology, Norwegian University of Science and Technology, Trondheim N-7491, Norway
[b] Department of Energy and Transport, SINTEF Ocean AS, Trondheim N-7491, Norway
[c] Norwegian Public Roads Administration, Oslo N-0667, Norway
[d] Department of Structural Engineering, Norwegian University of Science and Technology, Trondheim N-7491, Norway

ARTICLE INFO

Keywords:
Floating pontoon bridge
Coupled hydro-elastic dynamic analysis
Comparison to experiments
Wave and current response
Sensitivity study

ABSTRACT

The present paper provides a comparison between the numerical and experimental response for a generic floating pontoon bridge structure, thereby also serving to quantify the inherent uncertainties associated with both types of models. The numerical model is updated based on an initial comparison of static response and modal properties. The natural frequencies of the hydro-elastic model are calculated by also accounting for the frequency-dependent added mass of the pontoons. The model is then used to compare with the experiments for wave- and current-induced responses. The numerical model is subsequently applied for the purpose of quantifying the effect of uncertainties in the experimental model properties and setup. A clear description of the model details is given for reproducibility and experimental data is made available for future references.

The computer program used to create the numerical model has previously been validated for a wide range of different offshore structures, but such an assessment has not been made in connection with application to floating bridges. The objective of the present paper is accordingly to contribute to an improved understanding of hydro-elastic modelling capabilities e.g. in connection with future hybrid testing of such bridges that are characterised by significantly extended span-lengths.

1. Introduction

Confidence in the accuracy of the calculated dynamic response is imperative to the design of dynamically sensitive structures. For structural concepts such as floating bridges, it is particularly important to assess the uncertainties related to the calculated global response by comparing to either full-scale response of existing bridges or small-scale response from experiments. Furthermore, with the excessive length of the proposed floating bridge concepts for the ferry-free Coastal Highway Route E39 project in Norway of up to 4,600 m, future experiments are rendered infeasible due to scaling requirements and size limitations of existing ocean basins. In these cases it is necessary to perform so-called hybrid tests in the ocean basin, where a specific part of the bridge is scaled within scaling requirements and used to verify a numerical model. The verified numerical model is then used to estimate the response of the entire bridge, making the experimental results from such hybrid tests rely heavily on the performance of computer programs.

Different methods to assess the performance of numerical models have been applied to floating bridge structures over the years. Application of system identification methods for a submerged floating bridge tested in an ocean basin was described by Larssen et al. (1996), where the modal parameters were identified using a Covariance Block Hankel Matrix method and physical model parameters were estimated based on measured response and maximum likelihood estimates. In more recent years Petersen and Øiseth (2017) described a sensitivity-based finite element calibration method based on an analytical sensitivity matrix, which takes into account frequency-dependent system matrices due to the wave-structure interaction. By use of a system identification method with full-scale measurements of a floating pontoon bridge, the natural frequencies and mode shapes are calibrated. Kvåle et al. (2017) investigated the feasibility of three different system identification methods for the same floating pontoon bridge and found that a Covariance-driven Stochastic Subspace Identification method was the most promising method, although the high damping levels made the procedure challenging. For most general multi-purpose computer programs used in the offshore sector, system identification methods as the ones described above are not an integrated option and

* Corresponding author at: Department of Energy and Transport, SINTEF Ocean AS, Trondheim N-7491, Norway.
E-mail address: thomas.viuff@sintef.no (T. Viuff).

https://doi.org/10.1016/j.apor.2020.102368
Received 14 February 2020; Received in revised form 7 September 2020; Accepted 16 September 2020

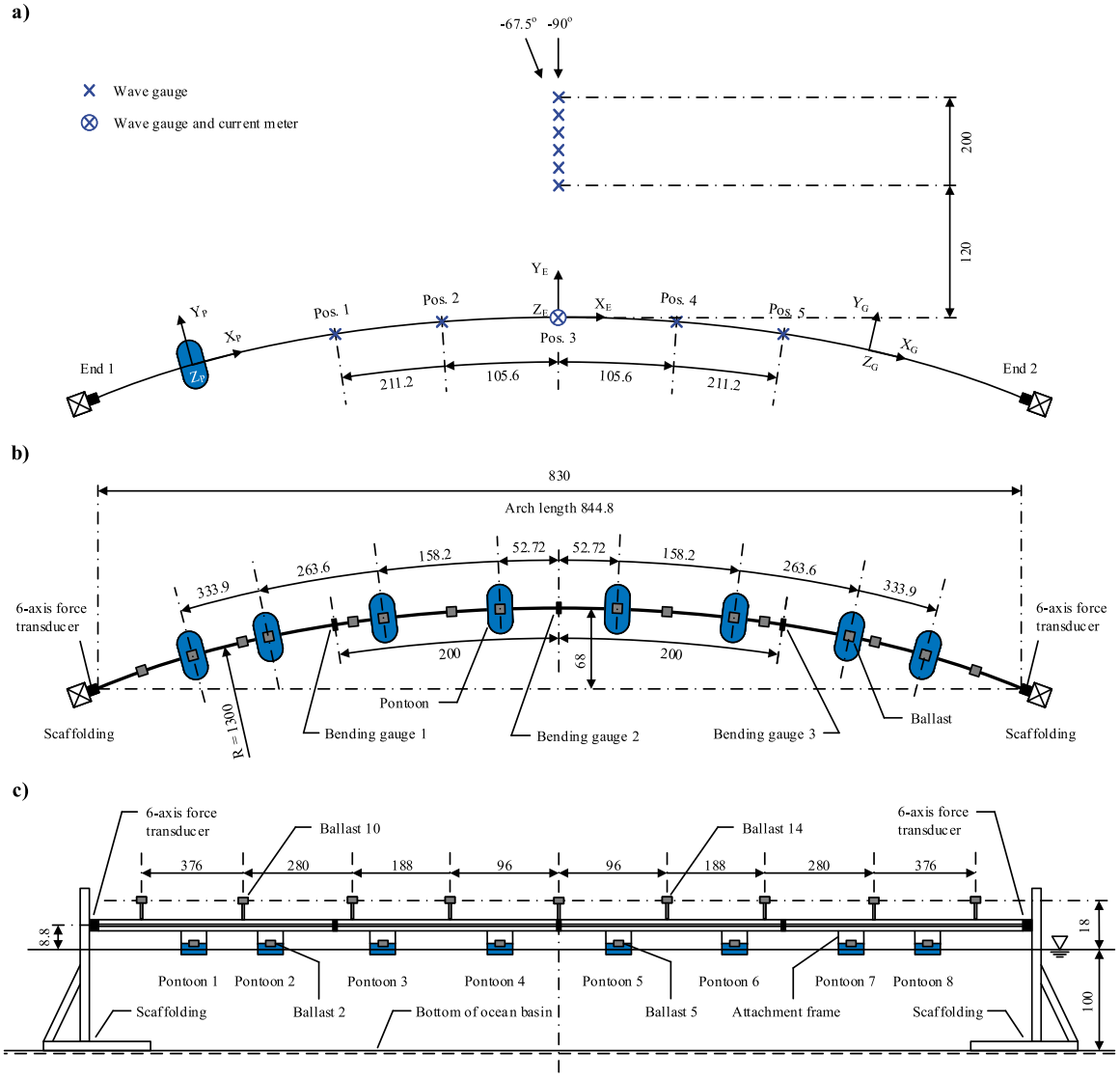

Fig. 1. Sketch of the experimental floating bridge model setup with all dimensions in m referring to full-scale. a) Top view of model with location of wave gauges, current meter, measurement positions Pos. 1 to 5, global coordinate system ($O_EX_EY_EZ_E$) with origo at the mean water line, local pontoon coordinate system ($O_PX_PY_PZ_P$) with origo at the mean water line and local bridge girder coordinate system ($O_GX_GY_GZ_G$) with origo at the center line of the bridge girder and wave directions θdefined according to the positive X_E-axis. b) Top view of model with locations of instrumentation and pontoons along the bridge. c) Side view of model with locations of traffic mass (ballast) along the bridge (horizontal distances are given as arch length). Sketch inspired by Løken and Oftedal (1990).

the model uncertainty assessment is instead carried out using sensitivity studies of the most important physical parameters.

In the present paper a model uncertainty assessment of the coupled hydro-elastic SIMO-RIFLEX SINTEF Ocean (2018a,b) program is presented. Previously, the computer program has been compared to others used in the offshore industry for different applications, see e.g. Viuff et al. (2020), Karimirad et al. (2011), Robertson et al. (2014), Sørum et al. (2017), but no information is available regarding experimental verification of the computer program when applied to floating pontoon bridge structures. The present paper compares a numerical model made in SIMO-RIFLEX version 4.14 to experiments carried out in 1989 by MARINTEK (now SINTEF Ocean) for a generic floating bridge structure. The description of the experimental model and the associated meassured response are based on two internal reports (Statens vegvesen, 1989; 1990) commissioned by the Norwegian Public Roads Administration (NPRA) and have been used in previous comparisons with other computer programs in the past, see Løken and Oftedal (1990) and Xiang and Løken (2019), who also verified the calculated hydrodynamic properties of the pontoons with experiments.

In Løken and Oftedal (1990) the numerical model was made up of hydrodynamic properties of the pontoons found using 3-dimensional radiation-diffraction theory, transferred to a linear beam model by an in-house algorithm. The dynamic equation was solved using a direct frequency-response method with one solution per wave frequency. Stochastic response was later derived using statistical methods in the post-processing of the data and all results were hence based on linear theory without including slow-drift, viscous drag or current. In Xiang and Løken (2019) a comparison of the results from three different numerical models was conducted. The three models applied a frequency-domain and a time-domain solution with no hydrodynamic interaction between the pontoons and a time-domain solution that included hydrodynamic interaction effects. Based on the comparisons the hydrodynamic interaction was found to have an effect on the vertical response of the bridge and for some frequencies fitted better to the experiments for beam sea. They also found that adding current to the numerical model had a dampening effect on the response opposite to the amplifying effect seen in the measured response.

Although the previous comparisons exists, they mostly describe the

experimental model and the findings of the comparison in overall terms with selected results for the comparison. Instead, the present paper gives a more detailed description of the experimental model and tries to show as much data as possible in the comparison. A meticulous case-by-case approach is employed in order to clarify the effect of different model uncertainties on the numerical model, including sensitivity tests on static response and natural frequencies in order to verify the fundamental properties of the numerical model. By manually implementing an iterative method to account for the frequency-dependent added mass of the pontoons, a closer match with the natural frequencies seen in measured response spectra is obtained, leading to a more trustworthy calibration of the the numerical model than in the previous comparison studies.

By validating the coupled hydro-elastic program to the experiments for a generic floating pontoon bridge, the present paper aims to 1) improve the confidence in the already existing body of research related to floating bridges based on the computer program, 2) increase the confidence in the performance of the program when considered for any potential future hybrid tests related to the proposed long floating pontoon bridges commissioned by the NPRA and 3) to be used as a reference for future computer program comparisons.

2. Experimental setup

The floating bridge is modelled in scale 1:40 making the model just shy of 22 m long, fitting inside the ocean basin with the dimensions 50 × 80 m. The model scale was at the time based on a trade-off between measurement accuracy, wave maker capacity and size requirements - including considerations towards reflected waves. Full-scale conditions are obtained using Froude scaling described in DNV (2010) with a water density factor of 1.025 and values given in this section will refer to full-scale conditions unless otherwise stated.

The bridge consists of a single horizontally curved beam (i.e. the bridge girder) supported by eight pontoons as illustrated in Fig. 1. The bridge is 830 m long with an arch length of 844.8 m and has a horizontal radius of 1,300 m. The center-line of the bridge girder is located at 8.8 m above the mean water level (MWL).

Three coordinate systems are used in the model, all of which are right-handed with the positive Z axes pointing upwards; the global Earth-fixed coordinate system ($O_EX_EY_EZ_E$) located at the middle of the bridge at the MWL, the local pontoon coordinate system ($O_PX_PY_PZ_P$) located at the center of each pontoon at the MWL with the $Y_P$axis perpendicular to the bridge curve, and the local bridge girder coordinate system ($O_GX_GY_GZ_G$) located at the center-line of the bridge girder cross-section with the $X_G$axis always tangent to the bridge girder.

The bridge girder consists of a single cross-section shaped as a cross with properties listed in Table 1. The length of the bridge girder is made up of four sections. The two sections closest to the middle are both 200 m long and the length of the other two is 222.4 m. Bending- and shear force gauges are inserted at the three assembly points between the four bridge sections to measure the bending moment around the local $X_G$and $Y_G$axes and shear force in the direction of those same axes. The mass of each gauge is 297.2 tonne and the dimensions are $L \times W \times H = 12$ m× 38 m× 16 m. The bending and torsional stiffness of the three gauges is relatively large compared to the bridge girder, although the details are unclear (Statens vegvesen, 1989). The two ends of the bridge (End 1 and End 2) are fixed in all translational degrees of freedom (DOFs). Torsional rotation around the $X_G$axis is restricted, while rotational springs with a spring stiffness of 196.8 MNm/deg are introduced for bending about the two other axes and the end forces are measured using a 6-axis force transducer at each end.

Eight identical pontoons are distributed along the bridge with varying distance from each other as sketched in Fig. 1. The pontoon geometry, projected onto the horizontal plane, is made up of a rectangle and two half circles. The total length, width and height of each pontoon is 45 m, 22 m and 4.3 m, respectively. From left to right the pontoons are numbered 1 to 8. The total distance of each pontoon from the middle of the bridge (the location of the $O_EX_EY_EZ_E$coordinate system) is given in Fig. 1 as arch length values. Each pontoon is rotated so as the positive $X_P$axis is tangent to the curvature of the bridge girder and the corresponding properties are listed in Table 2. The pontoons all have the same draft and are rigidly connected to the bridge girder using attachment frames.

Traffic load is included in the experimental setup using ballast at 17 different locations along the bridge girder, of which eight (Ballast 1–8) are located in the center of pontoon 1–8 at a height 1.816 m above the MWL. The other nine (Ballast 9–17) are spread out along the bridge girder at a height of 18.0 m above MWL corresponding to 9.2 m above the bridge girder center-line as illustrated in Fig. 1 and numbered from left to right. The mass properties of the traffic loads are listed in Table 3.

The motion response is measured in the experimental model at the five positions Pos. 1, 2, 3, 4 and 5 illustrated in Fig. 1 located at the 1/4, 3/8, 1/2, 5/8 and 3/4 spans along the arch length of the bridge, respectively. The force response is measured at the two ends (End1 and End2) as well as at Pos. 1, 3 and 5. A wave direction θ of -67.5° and -90.0° relative to the $X_E$axis is used, defined as positive when being counter-clockwise. In the verification of the numerical model the same wave directions and measurement points are used.

Six wave gauges are located 3–5 m in front of the bridge with equidistant steps of 0.4 m in order to measure the wave elevation. Six more wave gauges are located under the bridge at Pos. 1 to 5 and at the origo of the global Earth-fixed coordinate system. At the latter position, a current meter is also located in order to measure the current during the calibration tests before the bridge is put in the basin.

Table 1
Original bridge girder cross-sectional properties (Statens vegvesen, 1989).

Property	Unit	Full-scale
Mass	[tonne/m]	5.59E+00
Moment of inertia (Statens vegvesen, 1990)	[tonne · m^2/m]	6.69E+00
Radius of gyration (Statens vegvesen, 1990)	[m]	1.09E+00
Area	[m^2]	1.94E+00
Second moment of area (X_G)[a]	[m^4]	1.02E-01
Second moment of area (Y_G)	[m^4]	3.89E-01
Second moment of area (Z_G)	[m^4]	9.10E-01
Axial stiffness[b]	[kN]	5.48E+09
Weak axis bending stiffness[b]	[kN · m^2]	1.10E+09
Strong axis bending stiffness[b]	[kN · m^2]	2.57E+09
Torsional stiffness[c]	[kN · m^2/rad]	1.07E+08

[a] Based on measurements in small-scale.
[b] Based on $E = 69.0$ GPa for aluminium used in the model test.
[c] Based on $G = 22.5$ GPa for aluminium used in the model test.

Table 2
Pontoon properties based on Statens vegvesen (1989). Mass values refer to the center of gravity (COG) and does not include ballast. Stiffness values are defined relative to the local pontoon coordinate system ($O_PX_PY_PZ_P$) and the location of the COG is measured from the keel.

Property	Unit	Full-scale
Mass[a]	[tonne]	1.23E+03
Pitch inertia[a]	[tonne · m^2]	4.42E+04
Roll inertia[a]	[tonne · m^2]	1.47E+05
Yaw inertia[a]	[tonne · m^2]	2.40E+05
Draft[b]	[m]	2.58E+00
COG	[m]	3.30E+00
Displacement[b]	[tonne]	2.35E+03
Pitch water plane stiffness	[kN · m^2/rad]	3.21E+05
Roll water plane stiffness	[kN · m^2/rad]	1.25E+06
Heave stiffness	[kN/m]	8.92E+03

[a] The attachment frame is included in the pontoon mass.
[b] Based on final draft including ballast.

Table 3
Mass properties and vertical position of traffic load ballast and bending- and shear force gauges (Statens vegvesen, 1989).

Instrumentation	Z_E [m]	Mass [tonne]
Bending gauge 1–3	8.80E+00	2.97E+02
Ballast 1 & 8	1.82E+00	4.62E+02
Ballast 2 & 7	1.82E+00	1.21E+02
Ballast 3–6	1.82E+00	5.18E+01
Ballast 9–17	1.80E+01	2.18E+02

2.1. Tests carried out in the ocean basin

Several tests were carried out in the ocean basin, including static tests, decay tests, current, regular long-crested waves, irregular long-crested waves, short-crested waves, and a combination of current and irregular long-crested waves. The response measured for the listed test cases was presented as average values, standard deviations, maxima, minima, zero-up crossings, response spectra and response amplitude operators (RAOs) for the different responses measured at the seven positions along the bridge girder. Of the listed tests only results from selected tests are stated in Statens vegvesen (1989). Extra information is found in Statens vegvesen (1990). Of the given experimental results only some of them are reproduced in the present paper due to space considerations. See the section on supplementary material for link to an electronic appendix with most of the available experimental data and corresponding numerical comparison.

The static tests applied loads at the three positions along the bridge in both negative $Z_G$and $Y_G$direction and measured the translational displacements in the same three positions along the bridge each time.

Tests with regular waves were conducted for wave directions $\theta = -90°$and $-67.5°$, respectively, and the measured wave periods used for the RAOs were 4.00 s, 4.50 s, 4.94 s, 5.45 s, 6.03 s, 7.03 s, 8.05 s, 8.96 s, 10.47 s, 12.05 s and 13.46 s, of which the three lowest regular wave periods are close to the limits of the capability of the ocean basin facility (Næser, 1981).

The irregular wave tests compared in the present paper related to the hydro-elastic model tests are listed in Table 4. These tests include both long-crested waves, short-crested waves and finally, current and long-crested waves. The irregular waves generated in the experiments are assumed to be governed by the 3-parameter JONSWAP (Hasselmann et al., 1973) wave spectrum, which is parameterized by the significant wave height H_s, peak period T_p and the peak enhancement factor γ. The current velocity U_c is only present for test 533 and 534. The short-crestedness of the waves is modelled by means of the $\cos^s\theta$ spreading function based on information in Løken and Oftedal (1990), Statens vegvesen (1990).

Table 4
Measured wave parameters for irregular wave tests (Statens vegvesen, 1989).

Test no.	θ [°]	U_c [m/s]	H_s [m]	T_p [s]	γ[a] [-]	s [-]
530	−90.0	-	1.04	4.81	3.04	-
531	−90.0	-	1.44	4.93	3.33	-
532	−90.0	-	1.32	6.89	2.80	-
533	−90.0	0.92	0.96	4.74	3.19	-
534	−90.0	0.92	1.64	4.87	3.21	-
540	−90.0	-	0.96	4.87	3.62	2

[a] The peak enhancement factor γ is based on an assumed 1-to-1 relationship with the measured spectral peakedness parameter Q_P defined in Goda (1970).

2.2. Instrumentation and uncertainties

The instrumentation involved with the model tests include wave gauges, a current meter, 6-axis force transducers, bending- and shear force gauges and position gauges. The sampled data for all measurements is low pass filtered at 6 Hz (model-scale) before digitalization. The accuracy is stated to be 0.5% for the wave elevation, 2.0% for the current velocity, 0.5–1.0% for the 6-axis force transducers and bending- and shear gauges, and 0.01 mm for the position gauges, which is equivalent to 0.08 degrees for rotation measurements (Statens vegvesen, 1989).

As expected there are some uncertainties associated with tests carried out in the ocean basin laboratory related to accuracy in the measurements, precision in the positioning of the measurement equipment, wave maker proficiency, post-processing including signal filtering, and so on. The final accuracy of the experiments is estimated to 5–10% (Løken and Oftedal, 1990).

3. Numerical model

The numerical model illustrated in Fig. 2 is made in the coupled hydro-elastic program SIMO-RIFLEX. The theoretical background for all of the applied methods in the program is too extensive to cover in the present paper and instead only the most relevant information is given below for the sake of brevity. For more elaborate details the reader is referred to Viuff et al. (2019, 2020), SINTEF Ocean (2018a,b)

The program utilizes the finite element method (FEM) to idealize the structural system as a combination of linear beam elements and 6 degree of freedom (DOF) bodies with hydrodynamic properties and is able to solve static equilibrium equations, the eigenvalue problem as well as dynamic response in the time domain.

Frequency-dependent hydrodynamic properties of the bodies are included in the solution of the equation of motion through the hybrid frequency- and time-domain equation (Cummins, 1962).

$$q_j^{exc}(t) = \sum_{k=1}^{6} [M_{jk} + A_{jk}^{\infty}]\ddot{u}_k(t) + D_{jk}\dot{u}_k(t) + [K_{jk} + C_{jk}]u_k(t) + \int_0^{t_{mem}} k_{jk}(t-\tau)\dot{u}_k(\tau)d\tau \quad (1)$$

Here the structural mass, stiffness and damping properties are collected in the M_{jk}, K_{jk} and D_{jk} terms, respectively. The notation $q_j^{exc}(t)$is the wave excitation load on the 6 DOF bodies, including both linear first order wave load $q_j^{(1)}(t)$and viscous drag load $q_j^{(d)}(t)$,as functions of time t. The displacement response and the corresponding first and second order derivatives of time are given by the notations $u_k(t)$, $\dot{u}_k(t)$and $\ddot{u}_k(t)$. The angular frequency is denoted $\omega$and the indices are defined according to the body-fixed pontoon coordinate system with $j = 1, 2, ...,6$constituting surge, sway, heave, roll, pitch and yaw, respectively. The hydrostatic stiffness of the 6 DOF bodies are included in the term C_{jk}. The frequency-dependent potential damping is given by $b_{jk}(\omega)$. The frequency-dependent added mass $A_{jk}(\omega) = A_{jk}^{\infty} + a_{jk}(\omega)$is separated into a constant added mass at infinite frequency $A_{jk}^{\infty}$and a frequency-dependent part $a_{jk}(\omega)$. The hydrodynamic properties of the 6 DOF bodies are included through the retardation function $k_{jk}(t)$ seen in Eq. (2). This retardation function is multiplied with the response velocity for the same point in time and the resulting product is integrated from time zero to the "memory" time t_{mem} with a time lag τ.

$$k_{jk}(t) = \frac{1}{2\pi}\int_{-\infty}^{\infty}[b_{jk}(\omega) - i\omega a_{jk}(\omega)]e^{i\omega t}d\omega \quad (2)$$

In the above, the term i is the imaginary unit. The hydrodynamic properties of the pontoons are calculated in Wadam DNV (2014) based on 3-dimensional potential radiation and diffraction theory and the boundary element method (BEM) using a panel model of the pontoon geometry up to the MWL as seen in Fig. 3. The water density is set to 1.025 tonne/m^3 as that of saltwater and the draft of the pontoon is the

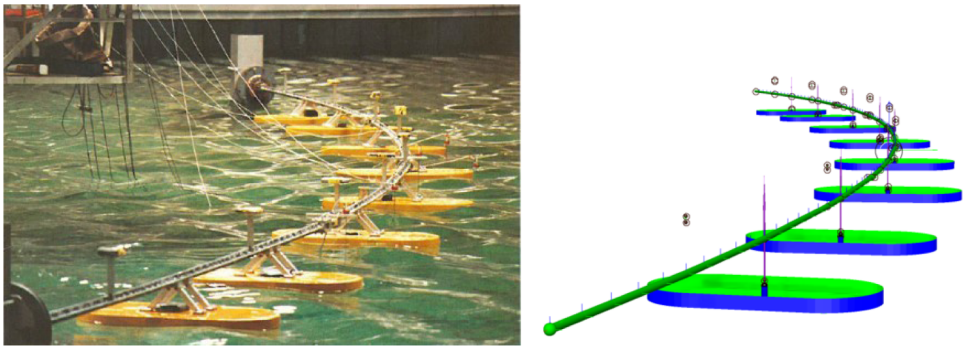

Fig. 2. Experimental model (Xiang and Løken, 2019) (left) and numerical model (right) of the generic floating bridge.

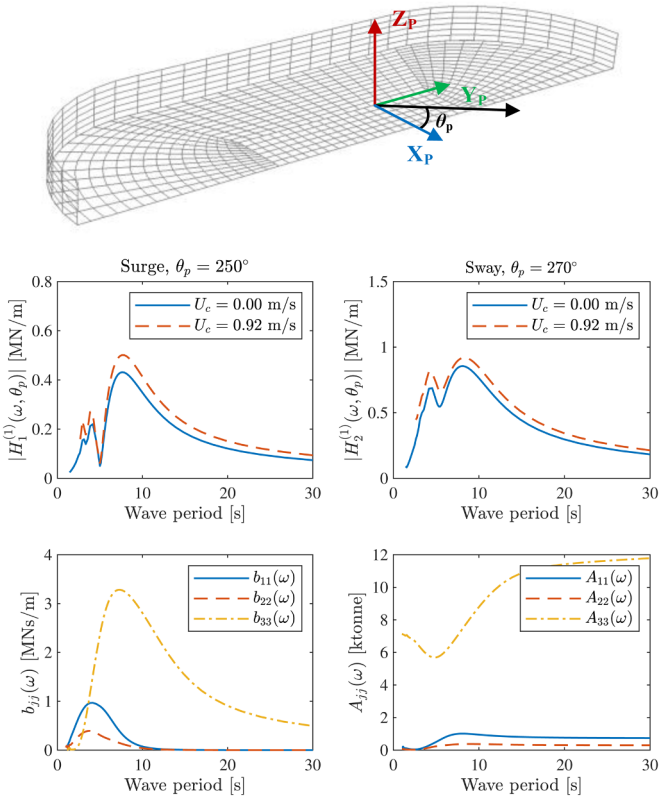

Fig. 3. Pontoon panel model with local coordinate system and wave direction notation θ_p (top) and hydrodynamic coefficients of pontoon 1 (bottom).

same as in the experiment using freshwater. This is done to make the scaled up values from the experiment and the numerical model fit using Froude scaling. Fig. 3 also shows the converged hydrodynamic coefficients based on the described panel model. The hydrodynamic interaction between the pontoons is neglected in the hydrodynamic analysis as a first approximation and no second order effects are considered due to no significant effects from slow drift excitation observed in the experiments (Løken and Oftedal, 1990).

3.1. Modelling first order wave loads

The time-dependent first order wave load $q_j^{(1)}(t)$is given in Eq. (3) based on the real part $\Re(\cdot)$ of the inverse fast Fourier transformation of the directional wave spectrum $S_\zeta(\omega_m, \theta_n)$ and the first order wave transfer function $H_j^{(1)}(\omega_m, \theta_n)$. The directional wave spectrum is simplified as the product of the unidirectional wave spectrum $S_\zeta(\omega_m)$ and the directional spreading function $D_\zeta(\theta_n)$.

$$q_j^{(1)}(x, y, t) = \Re \sum_{m=1}^{N_\omega} \sum_{n=1}^{N_\theta} \sqrt{2 S_\zeta(\omega_m) D_\zeta(\theta_n) \Delta\omega_m \Delta\theta_n}\, |H_j^{(1)}(\omega_m, \theta_n)| \exp\left[i \left(\varepsilon_{nm} + \varphi_{H_{jnm}^{(1)}} \right) \right] \exp[i(\omega_m t - k_m x \cos(\theta_n) - k_m y \sin(\theta_n))] \tag{3}$$

Here θ_n is the wave direction, ε_{nm} is a randomly generated phase angle, k_m is the wave number, x and y are coordinates of the pontoon bodies in the Earth-fixed global coordinate system and $\varphi_{H_{jnm}^{(1)}}$ is the phase angle of the first order wave force transfer function. The unidirectional wave spectrum is modelled as the 3-parameter JONSWAP wave spectrum with parameters listed in Table 4. See SINTEF Ocean (2018b) or Viuff et al. (2020) for the implementation in SIMO-RIFLEX. The directional spreading function $D_\zeta(\theta)$ in Eq. (4) is based on the Gamma function $\Gamma(\cdot)$, the main wave direction θ_0 and the spreading exponent s.

$$D_\zeta(\theta) = \frac{1}{\sqrt{\pi}} \frac{\Gamma(\frac{s}{2} + 1)}{\Gamma(\frac{s}{2} + \frac{1}{2})} \cos^s(\theta - \theta_0), \quad |\theta - \theta_0| \le \frac{\pi}{2} \tag{4}$$

3.2. Modelling viscous loads

Viscous drag loads are included in the numerical model using Morison elements at the center of each pontoon and Eq. (5), which is the drag term in the semi-empirical Morison equation.

$$q_j^{(d)}(t) = \frac{1}{2} \rho C_j^d A_j \dot{u}_r(t) |\dot{u}_r(t)| \tag{5}$$

Here ρ is the water density, $C_j^d$is the drag coefficient, A_j is the cross-sectional area, $\dot{u}_r(t)$is the relative velocity between the pontoon and the water and the index j is defined according to the body-fixed pontoon coordinate system with 1, 2 and 3 or interchangeably x, y and z indicating surge, sway and heave. The drag coefficients are based on values from the literature. Shao et al. (2019) has described a numerical investigation of the wave frequency pontoon response using both BEM and 2-dimensional computational fluid dynamics (CDF) software, and compared the results to experiments. The vertical drag coefficient is estimated to $C_z^d = 5.0$for a similar pontoon shape under comparable sea conditions. The horizontal drag coefficients are less understood and are in the present paper estimated to be $C_y^d = 1.0$and $C_x^d = 0.5$. The estimates for the horizontal drag coefficients are close to the values from DNV-RP-C205 DNV (2010)for Reynolds numbers close to 1e5 and values from Delany and Sorensen (1953) for Reynolds numbers close to 2.3e6, although both differ with roughly ± 50%. However, based on characteristic lengths of the pontoon of 22 and 45 m, a water temperature of 5 degrees and a measured current of 0.92 m/s in the experiment, the Reynolds numbers in the present study are in the proximity of 1.3e7 and 2.7e7, respectively, making the estimates somewhat uncertain.

3.3. Modelling structural damping

The structural damping ratio of the floating bridge model is estimated to $\xi_{struc} = 0.32\%$based on the aluminium used for the bridge girder cross-section (Statens vegvesen, 1990). The same structural damping ratio is achieved in the numerical model for the frequency range of the natural periods and the wave spectrum using Rayleigh damping with a mass proportional damping coefficient $\mu = 0.0031$and a stiffness proportional damping coefficient $\lambda = 0.0024$.

3.4. Wave-current interaction and second order effects

By use of the drag coefficients described above, the viscous effect of the pontoons is accounted for when computing the response for cases with current. For large-volume structures however, the wave-current interaction also changes the hydrodynamic coefficients. The effect on the first order wave force transfer function is accounted for in Wadam for each of the pontoons by specifying different forward speed vectors corresponding to the rotation of each pontoon and then solving the diffraction problem anew. In the applied version of Wadam it is not possible to solve the new radiation problem and for this reason changes to the added mass and potential damping are not accounted for. In the case with current and $T_p \approx 4.9$ s the ratio $U_c\omega_e/g \approx 0.135 \leq 1/4$ meaning that the current is considered small and the free-surface condition can be approximated with success in the BEM Faltinsen (1993). In the previous notation U_c is the current, $\omega_e = \omega_0 + \omega_0^2 U_c \cos\beta/g$is the wave encounter frequency, ω_0 is the angular wave frequency, β is the angle between the current and wave direction and g is the acceleration of gravity.

Although it was found by Zhao et al. (1988) that a current of 1 m/s increases the wave drift force by 50% for large-volume structures, the present paper does not include any second order effects. This choice is based on the fact that the contribution from the low-frequency response in the measured values was only 1–5% depending on the type of response (Statens vegvesen, 1990). By computing the response of test 534 listed in Table 4 with and without including second order effects such as wave drift forces and wave drift damping, the same 1–5% difference was found.

3.5. Other modelling details

The element length varies along the bridge girder due to modelling consideration such as the location of position gauges, pontoons and ballast, resulting in an element length of roughly 10 m corresponding to a total of 96 elements. The chosen number of elements is verified by an initial element length convergence study. The boundary conditions at the two ends are modelled using rotational springs and a combination of rigid body connections and nodal bodies are used to model the traffic load (ballast) above the bridge girder.

The connection between the bridge girder and the pontoons are modelled as rigid body connections to account for the stiff attachment frame used in the model test to connect the bridge girder and the pontoons. A buoyancy force is introduced in the center of buoyancy (COB) at each pontoon equivalent to the mass of the displaced water and in order not to count the roll and pitch restoring effect twice in the coupled analysis the buoyancy terms are removed from the hydrostatic stiffness matrix of the pontoon. The traffic load (ballast) located on the pontoons are modelled by adding fixed body elements with the corresponding mass and location data to each pontoon.

3.6. Solution procedures

The static solution procedure is based on a Newton-Raphson iterative procedure to find convergence for incremental load steps. Natural periods and mode shapes are found using the Lanczos Method and includes hydrostatic stiffness and added mass at infinite frequency of the pontoons by default. The hybrid frequency- and time-domain equation given in Eq. (1) are solved by applying an incremental formulation of the dynamic equilibrium equation and using the Newmark β-family integration method SINTEF Ocean (2018a). A slight amount of numerical damping is added by setting the integration parameters $\beta_{int} = 0.256$and $\gamma_{int} = 0.505$. This facilitates an earlier convergence and the effect on the dynamic response is negligible. The time-domain solution is made stable by ramping up the load for 100 s and utilizing a time step of 0.01 s based on a time step convergence study.

4. Results and discussion

The following sections contain a comparison of the numerical model with static tests conducted in the experiments, as well as a modal comparison of some of the natural periods observed in the experimental model, which are used to tune the numerical model. The RAOs for two wave directions are compared to the numerical results and a sensitivity study is performed for the drag coefficients. Stochastic response for both long-crested and short-crested waves is compared for the different tests listed in Table 4, including standard deviations and response spectra. Finally, the effect of applying a current is investigated and compared to the experiments.

The sensitivity towards different parameters is discussed in the following sections due to limited information available from the roughly 30 year old reports. The parameters are the modulus of elasticity E of the bridge girder cross-section material, orientation of the applied static load, rotational spring stiffness value at the two ends of the bridge, the weak and strong axis bending stiffness $EI_{Y_G}$and $EI_{Z_G}$of the bridge girder, torsional stiffness GI_{X_G},the radius of gyration r_{gyr} of the bridge girder, the wave direction θ, the drag coefficients values, and the structural damping ratio ξ_{struc}.

4.1. Verification of static response and modal properties

In the experiment a total of six static tests were carried out, three of which were conducted by placing weights equivalent to $F_{Z_G} = -6396$ kN at Pos. 1, 3 and 5. The other three used strings attached at the same three positions to pull with a static force of $F_{Y_G} = -6101$ kN in the horizontal direction perpendicular to the bridge axis. The relative displacement between the initial static position and the position when the loads were applied is illustrated in Fig. 4for both experimental and numerical response. In the experimental setup the horizontal load directions were not perfectly perpendicular to the bridge girder, with an offset *OSC* of 40–80 m from the centre of the bridge girder arc, reported in Statens vegvesen (1989). An offset *OS*3 of 12 m in the load attack point at Pos. 3 in the positive $X_G$direction is also reported for the applied horizontal force in the static tests, which is included in the numerical model.

Based on a comparison of the static displacements, the sensitivity towards the modulus of elasticity of the bridge girder cross-section E of roughly 1.6% is checked and found insignificant. Similarly, a low sensitivity to the offset *OSC* in the horizontal force direction is found. The static comparison shown in Fig. 4 implies that the experimental model is slightly stiffer than the numerical model in both the vertical and horizontal directions. The relatively large differences in the measured and calculated displacements of the structure is thought to be related to the, in relative terms, larger stiffness of the bending- and shear force gauges. Another less likely reason is uncertainty in the spring stiffness value of the inserted rotational springs at the two ends. To check both scenarios, a sensitivity test is carried out for both bridge girder bending stiffness and the rotational spring stiffness at the two ends. The bridge girder bending stiffness is changed with a modifier f_{EI} of 1.00, 1.10 and 1.20 multiplied with the original cross-section properties listed in Table 1. Likewise, the rotational spring stiffness at the two ends is changed with the modifier f_{BC} of 1.00, 2.00 and 4.00 multiplied with the original rotational spring stiffness of 196.8 MNm/deg. A change in

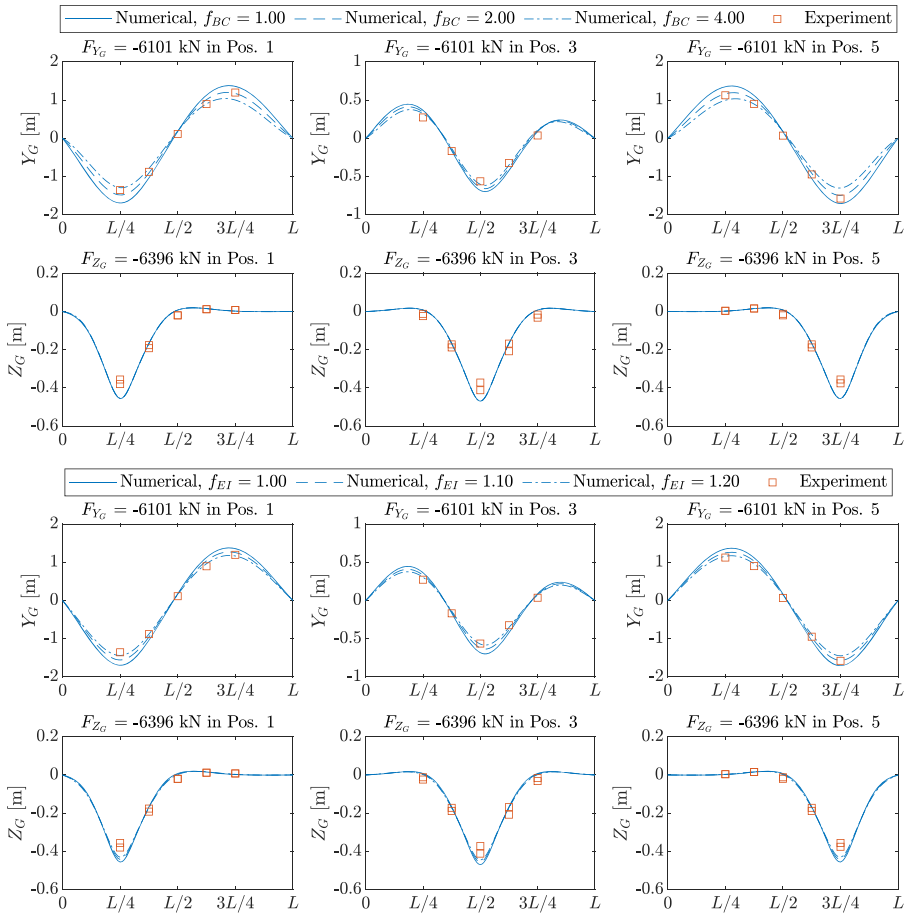

Fig. 4. Displacement comparison for different static conditions at the five measured positions in the model test (Statens vegvesen, 1989) and the numerical model along the arch length L of the bridge. Sensitivity study with respect to the modifier f_{BC} applied to the rotational spring stiffness at the boundary conditions (top) and sensitivity study with respect to the bridge girder bending stiffness modifier f_{EI} (bottom). Base case: OSC = 0 m, $OS3$ = 12 m, f_{BC} = 1.00and f_{EI} = 1.00.

the horizontal displacement is observed when changing f_{BC}, while the vertical displacement is almost unchanged. On the contrary, both the horizontal and vertical static response is sensitive to changes of f_{EI}. Based on the value of f_{EI} and f_{BC}, the structure is most sensitive to changes in the bridge girder bending stiffness properties.

The modal properties are estimated in the numerical model using added mass at infinite frequency matrices for the pontoons. By manually running an iterative procedure the modal comparison can be forced to include the frequency-dependent added mass of the pontoons: a) calculate the natural angular frequencies based on the added mass at infinite frequency matrices of the pontoons, b) update the added mass at infinite frequency matrices to include the added mass at the newly calculated natural angular frequencies, c) continue step a, and b until the difference between the angular natural frequencies used to obtain the input added mass and the natural frequencies obtained from the last run are within a specified tolerance level. The final natural periods obtained from this iterative procedure are listed in Table 5. The notation Y2 in the table is for the first horizontal mode consisting of two half sine waves, Z1 is the first vertical mode consisting of a single half sine wave and RX1 is the first rotational mode with a single half sine wave. The natural periods of the experimental model are based on decay tests and vertical and horizontal displacement RAOs from test 532, see Fig. 5. The natural period of the first horizontal mode Y2 is compared to the model test value of 9.96 s and shows an original difference of roughly 6%. The same difference is observed between the second horizontal mode Y3 and the model test value of 4.95 s based on response spectra for test 532. Changing the bending stiffness of the bridge girder cross-section with the modifier f_{EI} = 1.16corresponding roughly to an increase of the frequency by a factor of 1.06^2 gives a good match for the first two horizontal modes. The vertical modes are also changed, although not as much, due to the relatively large pontoon heave stiffness.

Table 5
Comparison of modal properties of the experimental model with that of the numerical model using different modifiers f. Frequency-dependent added mass is taken into account manually.

Mode	f_{BC} = 1.00		f_{BC} = 1.00		Exp. Statens vegvesen (1989, 1990)	
	f_{EI} = 1.00		f_{EI} = 1.16		Value	Diff
n	Shape	[s]	Shape	[s]	[s]	[%]
1	Y2	10.59	Y2	9.98 [a]	9.96	0.2
2	Z1	7.89	Z1	7.88	7.85	0.4
3	Z2	7.70	Z2	7.67	7.35	4.4
4	Z3	7.17	Z3	7.09	6.87	3.2
5	Z4	6.24	Z4	6.09	-	-
6	Y3	5.32	RX1	5.11	5.53	-7.6
7	RX1	5.11	Y3	4.98	4.95	0.5
8	Z5	5.10	Z5	4.90	-	-
9	RX2	4.56	RX2	4.55	4.82	-5.6
10	RX3	4.01	RX3	3.99	-	-
11	Z6	3.93	Z6	3.73	-	-
12	RX4	3.68	RX4	3.65	-	-
13	RX5	3.23	RX5	3.22	-	-
14	Z7	3.04	RX6	2.91	-	-

[a] Numerical decay test returns 10.00 s.

The persisting difference in the natural periods of the vertical modes could be related to imperfections of the pontoon shapes in the experiment. The natural periods of the rotational modes are, as expected, practically unchanged by the mentioned modifications.

To obtain the same match in the first horizontal mode the rotational spring stiffness at the two ends of the bridge has to be changed with a modifier f_{BC} = 1.79with only slight changes to the other modes. The natural periods of the first two torsional modes are roughly 7% lower

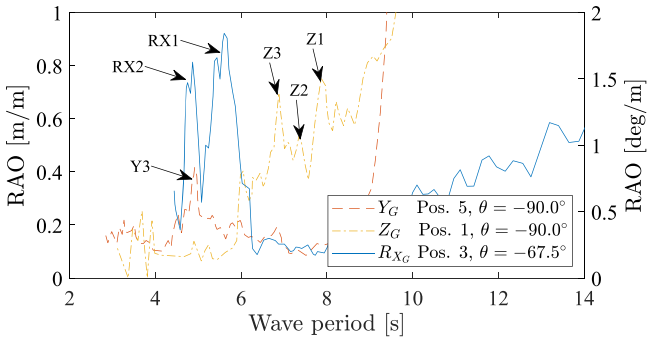

Fig. 5. Observable modes of the experimental model (Statens vegvesen, 1989; 1990) in the displacement and rotation RAOs based on long-crested irregular waves

than those observed in the RAO for torsion. This does not fit with the relatively larger torsional stiffness of the bending and shear force gauges mentioned earlier and when changing the torsional stiffness with ± 20% the natural period of the first torsional mode is changed by less than 1%. For this reason, no modification of the torsional stiffness has been done. Similarly, no change to the radius of gyration of the bridge girder cross-section has been made. Assuming that the mass of the inserted shear and bending gauges is equally distributed over their dimensions, the radius of gyration of the bridge girder is increased by 46%, which is an insignificant change when compared to the contribution from the pontoons. Based on the previous sensitivity studies in both static and eigenvalue calculations, the bridge girder bending stiffness modifier is kept at $f_{EI} = 1.16$and the rotational spring stiffness modifier at the two ends is kept at $f_{BC} = 1.00$unless otherwise stated.

4.2. Potential damping from pontoons

With a structural damping ratio $\xi_{struc} = 0.32\%$the potential damping from the pontoons are more likely to influence the amplitude of the response at resonance periods in general. A potential damping ratio $\xi_{pot,n}$ for mode n can be found using Eq. (6).

$$\xi_{pot,n} = \frac{N_p \cdot b(\omega_n)}{2[M_S + N_p \cdot A(\omega_n)]\omega_n} \tag{6}$$

Where, M_S is the total dry mass of the structure, $b(\omega_n)$ and $A(\omega_n)$ are the relevant hydrodynamic potential damping and added mass at the angular frequency ω_n for mode n, respectively, and N_p is the number of pontoons. The potential damping ratio for e.g. vertical mode n can be calculated based on Eq. (6) by taking the structural mass listed in Tables 1 and 2, together with the hydrodynamic added mass $A_{33}(\omega_n)$ and potential damping $b_{33}(\omega_n)$ shown in Fig. 3 related to the natural frequency ω_n of the mode. Doing so, the potential damping ratios at the first five vertical modes are between 24% and 28% and these are thought to be unaffected by other types of damping in the model. The potential damping ratios for the first and second horizontal mode is roughly 8% and 52%, respectively, and the response amplitudes at the wave periods corresponding to the first mode are more likely to be influenced by a correct modelling of the damping in the system.

4.3. Regular wave global response

The RAOs from the model test are compared with the computed response in Fig. 6 for the two ends and at Pos. 1, 3 and 5 and show that the computed response in general follow the experiments well. Even at the low periods where a high uncertainty is present in the experimental results as described above, the behaviour is captured to a satisfying level.

Due to imperfections in the experimental tests such as the accuracy of the orientation of the model and the long-crested regular wave generation, the first horizontal mode Y2 is excited, which is not the case for the numerical model where the mode is cancelled out due to the idealised symmetry of the bridge. Based on Statens vegvesen (1989), the accuracy in the wave direction in the experiments is 0.4°. By changing the wave direction in the numerical model by 0.5°, the mode is observed in several of the computed RAOs. The fact that this floating bridge concept is highly sensitive to the wave direction is not a new finding but has been discussed in many previous studies, see e.g. Viuff et al. (2019), Villoria (2016), Langen and Sigbjörnsson (1980).

The weak axis bending moment M_{Y_G}shows a good comparison with a clear coupling to the vertical displacement around the first four vertical modes. The strong axis bending moment M_{Z_G}follow the behaviour of the horizontal displacement RAOs and show a bump in the amplitude at 10 s corresponding to mode Y2. This bump is also present in the RAO for R_{X_G}at Pos. 3 and is thought to be a result of the coupling between pitch of the pontoon and the horizontal motion of the bridge girder.

The axial force F_{X_G},the torsional moment M_{X_G},the vertical shear force $Q_{Z_G}$and horizontal shear force Q_{Y_G}RAOs are shown for the two ends of the bridge and overall show a good match for both wave directions. The torsional moment is slightly under predicted by the numerical model but follow the same general behaviour as that of the experiment.

Other results such as the vertical and horizontal shear force RAOs at Pos. 1, 3 and 5 are also compared but omitted here due to space considerations. Similar to the torsional moment, the shear force is slightly lower than the measured values with a difference of up to 30% for $\theta = -67.5°$. In the case of the measured shear forces, a reported uncertainty of up to 65 kN persists in the measurd values (Statens vegvesen, 1989). With low shear force values at the middle of the bridge in beam sea, the uncertainty makes up roughly 50% of the measured response.

Other possible reasons for discrepancies is the hydrodynamic interaction between the pontoons not being taken into account in the numerical model. Xiang and Løken (2019) have shown, using a different hydro-elastic program, that for this particular bridge the hydrodynamic interaction has an impact on the vertical motion RAOs.

4.3.1. Sensitivity towards drag coefficient values

Some uncertainty is tied to the drag coefficients used to model the viscous drag around the pontoons. To evaluate the importance of these coefficients a sensitivity study is performed using ± 50% of the initial values for both −89.5° and −67.5° wave directions and the corresponding results are shown in Fig. 6 as the shaded areas. Only small changes in the structural response is present at the lower wave periods and around mode Y2. Generally an insignificant effect is found, which is partly due to the high amounts of potential dampening from the pontoons. Another reason is the relatively small vertical motion of the bridge, resulting in low viscous damping effects.

4.3.2. Sensitivity towards structural damping ratio

As discussed in the previous sections, mode Y2 has a relatively low potential damping ratio making other damping contributions more important. To check the influence from structural damping on the system, four simulations with regular waves from −90.0° and −67.5° and wave periods corresponding to mode Y2 and Y3 are conducted based on $\varepsilon_{struc} = 0.50\%$. The resulting RAOs are marked in Fig. 6and the results are almost identical to the response based on $\varepsilon_{struc} = 0.32\%$.

4.4. Long-crested irregular wave global response

A comparison between standard deviations of the measured response and the computed response based on three different wave directions is listed in Table 6. The factor in the table is defined as the standard deviations of the computed response divided with the corresponding measured values and the computed standard deviations are based on 10 3-hour simulations in order to achieve convergence.

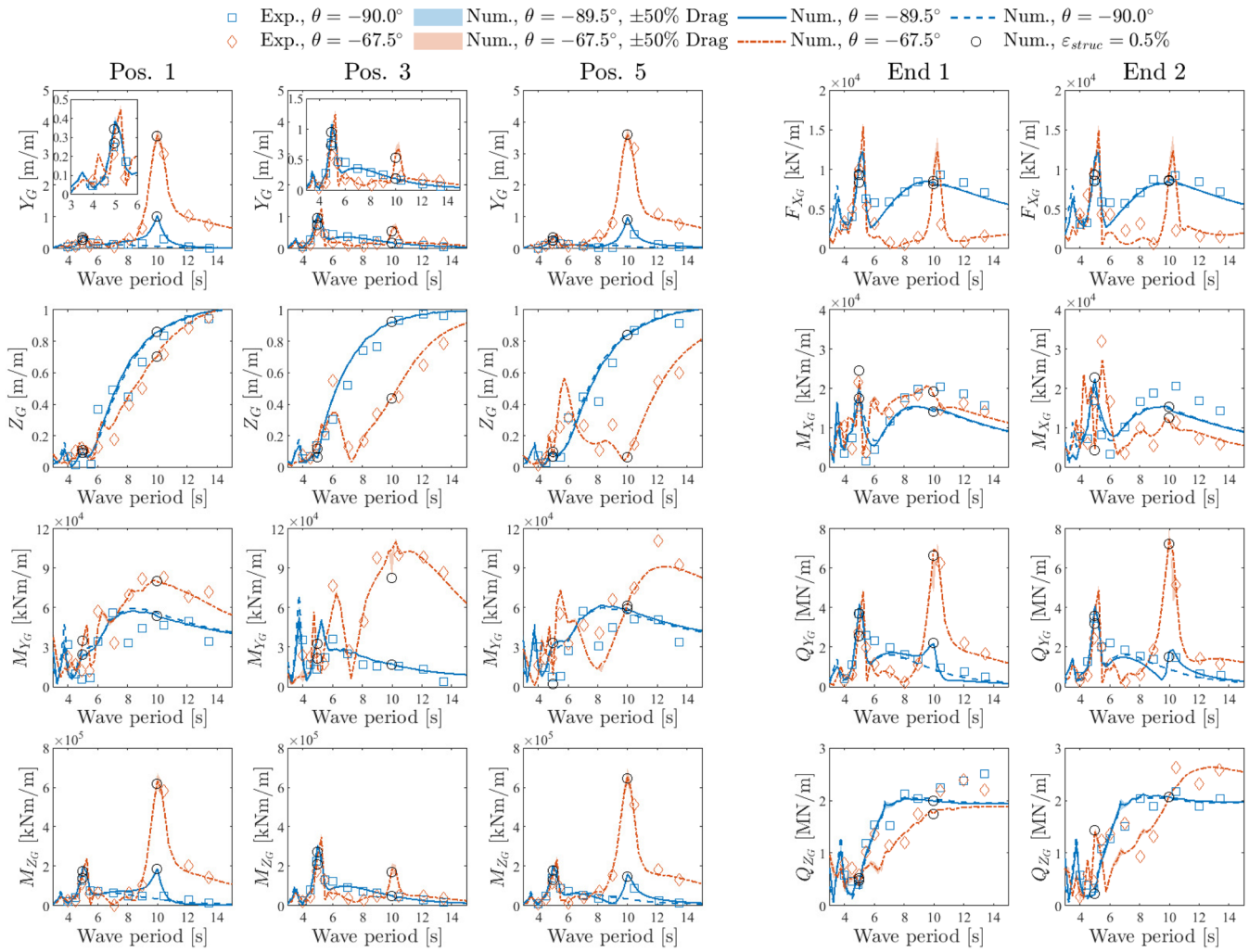

Fig. 6. Comparison of regular wave RAOs at Pos. 1, 3 and 5 (left) and End 1 and 2 (right) for two wave directions θ in experiment (Statens vegvesen, 1989; 1990) versus the numerical model

As a first observation, the horizontal response types Y_G, $M_{Z_G}$and Q_{Y_G}show a higher sensitivity towards the wave direction than the vertical response types Z_G, $M_{Y_G}$and Q_{Z_G},which can explain most of the differences between the experiment and the numerical model. Fig. 7 highlights the directional sensitivity in the corresponding response spectra of the horizontal response types and also R_{X_G}at locations along the bridge where they are most influenced. It is clear that the energy around the first horizontal mode Y2 is strongly influenced by the small changes in the wave direction. The mode is clearly present in the measured response spectra, while it is only present in the response spectra from the computed response types for wave directions -89.0° and -89.5° due to the symmetrical properties of the numerical model. The shapes of the response spectra compare best at -89.5°. This is also seen in the factors listed in Table 6, where the standard deviations of the computed horizontal response fit best at that particular wave direction. Looking at the average factor for each response type over all the listed positions for -89.5°, the horizontal response types Y_G, $M_{Z_G}$and $Q_{Y_G}$are within 1%, 7% and 20% of the experiment. Some of the remaining differences for the horizontal response types are related to the energy in the response spectra around mode Y3, where the numerical model have relatively larger amplitudes, depending on the response type. The energy around this mode, however, does not seem to be affected by changes in the wave direction.

The average factor for the vertical response types Z_G, $M_{Y_G}$and $Q_{Z_G}$for -89.5°, are within 4%, 12% and 38% of the experiments, respectively. The largest outlier is the vertical shear force at Pos. 3, with a factor of 0.28. This is mainly connected to the uncertainty of 65 kN in the measurements combined with the relatively small standard deviation values at this position equivalent to 0.01% of the yield stress capacity of the bridge girder cross-section used in the experiment. Excluding this outlier then the average Q_{Z_G}response is only 22% lower than that of the experiment, with the best comparison at the two ends of the bridge. This uncertainty also influences the measured Q_{Y_G}response at Pos. 3.

The torsional rotation $R_{X_G}$of the bridge seems to compare poorly with an average factor of 1.29 along the bridge and with a factor of 1.54 at Pos. 3 for -89.5°. Furthermore, the response shows a low sensitivity towards changes in the wave direction. From Fig. 7 it seems that the numerical model overestimates the torsional response at the peak period of the wave spectrum and at mode RX2 for beam sea. The accuracy of the rotation measurements are however 0.08°, corresponding to 21–30% of the measured values (Statens vegvesen, 1989). A similar study (Xiang and Løken, 2019) between the same experiment and another numerical software found similar differences in the torsional rotation response.

The axial force $F_{X_G}$and the vertical shear force Q_{Z_G}at the two ends of the floating bridge show a low sensitivity towards the wave direction and are both well within the 10% uncertainty related to the measurements. Instead, the torsional moment $M_{X_G}$is roughly 17% different and

Table 6
Comparison of standard deviations for test 532 highlighting the directional sensitivity. The factor is defined as numerical/experiment value.

Response	Position	Unit	Exp. Statens vegvesen (1989)	Numerical			Factor		
				−89.0°	−89.5°	−90.0°	−89.0°	−89.5°	−90.0°
Y_G	Pos. 1	[m]	6.34e-02	8.88e-02	6.50e-02	4.88e-02	1.40	1.02	0.77
Y_G	Pos. 3	[m]	1.33e-01	1.35e-01	1.36e-01	1.37e-01	1.02	1.02	1.03
Y_G	Pos. 5	[m]	5.37e-02	6.83e-02	5.03e-02	4.88e-02	1.27	0.94	0.91
Z_G	Pos. 1	[m]	1.37e-01	1.32e-01	1.26e-01	1.21e-01	0.96	0.92	0.88
Z_G	Pos. 3	[m]	1.66e-01	1.74e-01	1.76e-01	1.77e-01	1.05	1.06	1.06
Z_G	Pos. 5	[m]	1.27e-01	1.08e-01	1.14e-01	1.21e-01	0.85	0.90	0.95
R_{X_G}	Pos. 1	[deg]	2.88e-01	3.66e-01	3.44e-01	3.23e-01	1.27	1.19	1.12
R_{X_G}	Pos. 3	[deg]	3.75e-01	5.80e-01	5.81e-01	5.81e-01	1.55	1.55	1.55
R_{X_G}	Pos. 5	[deg]	2.70e-01	2.84e-01	3.03e-01	3.23e-01	1.05	1.12	1.20
M_{Y_G}	Pos. 1	[kNm]	1.51e+04	1.34e+04	1.38e+04	1.43e+04	0.88	0.91	0.95
M_{Y_G}	Pos. 3	[kNm]	1.18e+04	8.44e+03	9.28e+03	9.76e+03	0.71	0.79	0.83
M_{Y_G}	Pos. 5	[kNm]	1.55e+04	1.49e+04	1.47e+04	1.44e+04	0.96	0.95	0.93
M_{Z_G}	Pos. 1	[kNm]	2.49e+04	2.89e+04	2.66e+04	2.50e+04	1.16	1.07	1.00
M_{Z_G}	Pos. 3	[kNm]	3.61e+04	3.73e+04	3.76e+04	3.77e+04	1.03	1.04	1.04
M_{Z_G}	Pos. 5	[kNm]	2.20e+04	2.48e+04	2.44e+04	2.50e+04	1.13	1.11	1.14
Q_{Z_G}	Pos. 1	[kN]	3.11e+02	2.25e+02	2.36e+02	2.46e+02	0.72	0.76	0.79
Q_{Z_G}	Pos. 3	[kN]	1.71e+02	5.59e+01	4.82e+01	4.00e+01	0.33	0.28	0.23
Q_{Z_G}	Pos. 5	[kN]	3.13e+02	2.60e+02	2.51e+02	2.43e+02	0.83	0.80	0.78
Q_{Y_G}	Pos. 1	[kN]	4.16e+02	3.92e+02	3.95e+02	3.96e+02	0.94	0.95	0.95
Q_{Y_G}	Pos. 3	[kN]	1.24e+02	1.08e+02	7.47e+01	6.22e+01	0.87	0.60	0.50
Q_{Y_G}	Pos. 5	[kN]	4.06e+02	3.48e+02	3.48e+02	3.41e+02	0.86	0.86	0.84
F_{X_G}	End 1	[kN]	2.08e+03	1.92e+03	1.91e+03	1.91e+03	0.92	0.92	0.92
F_{X_G}	End 2	[kN]	2.07e+03	1.86e+03	1.88e+03	1.91e+03	0.90	0.91	0.92
Q_{Y_G}	End 1	[kN]	7.22e+02	6.22e+02	5.92e+02	5.59e+02	0.86	0.82	0.77
Q_{Y_G}	End 2	[kN]	6.64e+02	5.06e+02	5.31e+02	5.59e+02	0.76	0.80	0.84
Q_{Z_G}	End 1	[kN]	5.42e+02	4.99e+02	5.02e+02	5.05e+02	0.92	0.93	0.93
Q_{Z_G}	End 2	[kN]	4.96e+02	4.96e+02	5.02e+02	5.05e+02	1.00	1.01	1.02
M_{X_G}	End 1	[kNm]	4.41e+03	3.52e+03	3.56e+03	3.64e+03	0.80	0.81	0.83
M_{X_G}	End 2	[kNm]	4.36e+03	3.88e+03	3.73e+03	3.65e+03	0.89	0.86	0.84

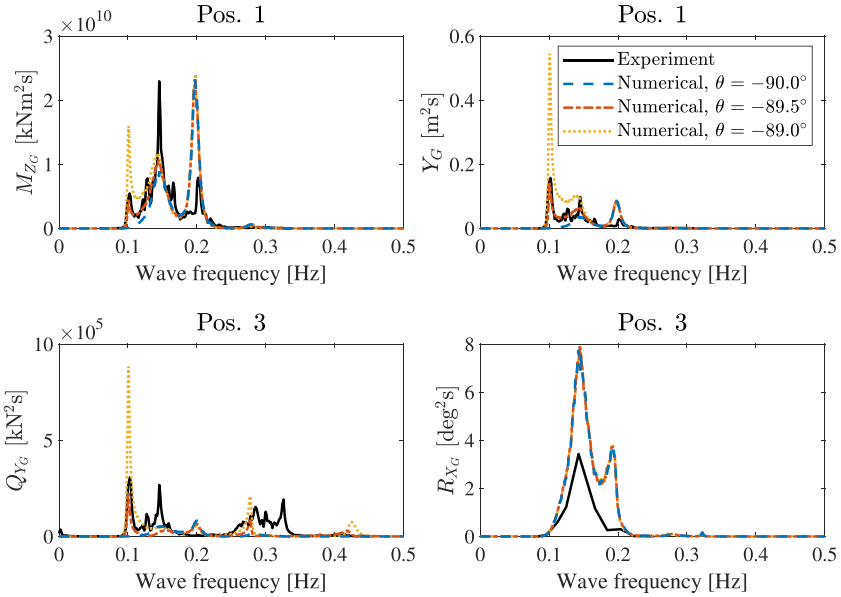

Fig. 7. Directional sensitivity in response spectra for long-crested irregular wave test 532 (Statens vegvesen, 1989; 1990).

is thought to be linked to the discrepancies observed for the torsional rotation.

Other less significant sources of error is the presence of transient effects such as slamming which was present during the experimental tests, especially for beam sea (Statens vegvesen, 1990). This effect is not included in the numerical model.

4.5. Short-crested irregular wave global response

Short-crested sea was investigated using the directional spreading function in Eqn. (4), with the spreading exponent $s = 2$and the main wave direction $\theta_0 = -90.0°$according to Table 4. In the experiments a total of up to 120 wave directions is possible using a *snake wave spectrum* (Næser, 1981) although the exact number used is uncertain. The

Table 7
Comparison of standard deviations for test 540. The factor is defined as numerical/experiment value and the numerical model is based on $\theta_0 = -89.5°$.

Resp.	Pos.	Unit	Exp. Statens vegvesen (1990)	Num.	Fac.
Y_G	Pos. 1	[m]	3.60e-02	4.00e-02	1.11
Y_G	Pos. 2	[m]	5.40e-02	5.22e-02	0.97
Y_G	Pos. 3	[m]	9.20e-02	9.62e-02	1.05
Z_G	Pos. 1	[m]	3.80e-02	4.50e-02	1.18
Z_G	Pos. 2	[m]	4.60e-02	4.73e-02	1.03
Z_G	Pos. 3	[m]	4.50e-02	4.50e-02	1.00
R_{X_G}	Pos. 3	[deg]	2.35e-01	3.10e-01	1.32
Q_{Z_G}	Pos. 1	[kN]	1.70e+02	1.66e+02	0.97
Q_{Z_G}	Pos. 3	[kN]	2.03e+02	1.59e+02	0.78
Q_{Y_G}	Pos. 1	[kN]	2.63e+02	2.56e+02	0.97
Q_{Y_G}	Pos. 3	[kN]	1.07e+02	1.05e+02	0.98
M_{Y_G}	Pos. 1	[kNm]	7.84e+03	8.24e+03	1.05
M_{Y_G}	Pos. 3	[kNm]	9.56e+03	9.55e+03	1.00
M_{Z_G}	Pos. 1	[kNm]	1.71e+04	1.85e+04	1.08
M_{Z_G}	Pos. 3	[kNm]	2.78e+04	2.75e+04	0.99
F_{X_G}	End 1	[kN]	1.23e+03	1.41e+03	1.14
Q_{Y_G}	End 1	[kN]	4.35e+02	3.81e+02	0.88
Q_{Z_G}	End 1	[kN]	2.11e+02	1.97e+02	0.93
M_{X_G}	End 1	[kNm]	3.58e+03	3.71e+03	1.04

default option in SIMO-RIFLEX is to specify an odd number of wave directions in the spreading function, although the option for manually defining a directional wave spectrum is also available. In the present paper the computed results are based on 101 equally distributed wave directions, although 12 was used in the numerical model in Statens vegvesen (1990).

A comparison of the response standard deviations is given in Table 7 showing a good agreement between computed and measured reponse in short-crested waves. Here, the main wave direction is $-89.5°$, although changes in the response when compared to waves from $-90.0°$ is within 2%, which indicates that the response in short-crested waves is less sensitive to changes in the main wave direction. This is supported by Viuff et al. (2019) who showed a low sensitivity in the extreme response of a longer but similar floating pontoon bridge for main wave directions within 15° from beam sea. A check using 11, 12, 13 and 51 wave directions indicate that although the average difference between the response and the experiment is within 5% for all four tests, then the difference at each individual response varies more as the number of wave directions decrease. When comparing the numerical results based on 101 wave directions to the same simulations based on 51, 13, 12 and 11 wave directions, the maximum difference in the individual response types is found to be within 2%, 7%, 6% and 5%, respectively.

4.6. Comparison of the current-wave interaction effect

Table 8 lists the measured and computed response standard deviations for test 530, 531, 533 and 534 normalized by the corresponding measured H_s values listed in Table 4. These tests are based on varying H_s and U_c values and the normalized results indicate the influence from current for cases with similar wave heights as well as the influence from increasing wave height for cases with and without current. By comparing response standard deviations normalized to the corresponding H_s values of each test, it helps to make the comparison more clear.

The effect of increasing the significant wave height for cases without current can be checked by comparing test 531 to 530. Similarly, it can be checked for cases with current by comparing test 534 to 533. In the case without current an increase in the averaged normalized response is found to be roughly 7% when increasing H_s with roughly 39%. A roughly 6% increase is present when increasing H_s with roughly 71% for the case with current. The corresponding effect in the numerical model is 8% and 9% for cases without and with current, respectively. According to Statens vegvesen (1990) they found a 17% increase in the experimental response with increasing H_s for cases with current, although this was found by comparing normalized stochastic responses that were normalized with the specified H_s values and not the actual measured ones listed in Table 4.

The effect of adding current to long-crested waves with low H_s can be checked by comparing test 533 to 530. An average increase in the normalized response of 18% is found in the experiments and the corresponding increase in the numerical model is 4%. Similarly, the effect of adding current to long-crested waves with high H_s can be checked by comparing test 534 to 531. Here the experiments give an increase in the averaged normalized response of 17%, while for the numerical model this value is 5%.

5. Conclusion

An extensive model uncertainty assessment and experimental verification of a coupled hydro-elastic program is presented for wave- and current-induced global response of a 830 m long end-anchored floating pontoon bridge.

An assessment of the sensitivity (effect) in the computed static and modal results is carried out for a list of known experimental model uncertainties. The list includes static horizontal load orientation (low), bridge girder bending stiffness (high), rotational spring stiffness at the two ends (medium), bridge girder torsional stiffness (low) and bridge girder torsional inertia (low). An agreement in static and modal properties is achieved by increasing the original bridge girder bending stiffness with 16% due to the relatively larger bending stiffness of the bending and shear force gauges inserted at the 1/4, 1/2 and 3/4 span of the bridge in the experiment. With the increased bending stiffness, the computed natural periods of the first three vertical modes and the first two horizontal modes corresponds to the peaks observed in the response spectra from the experiments with an accuracy within 5% and 1%, respectively. Differences of up to 8% exists for torsional modes.

The response amplitude operators (RAOs) are compared between the experimental model and time domain results for two wave directions showing a good agreement. Due to the symmetrical shape of the first horizontal mode, a high sensitivity towards the long-crested wave direction is found in the horizontal response close to beam sea, which explains most of the differences between the calculated and measured response. Variations in the applied drag coefficients of $\pm$ 50% generally has a low effect on the calculated response. Only response related to the first horizontal mode is slightly affected. Similarly, a low sensitivity towards the structural damping ratio is found in the response. This is assumed to be a consequence of the high amount of potential damping at the pontoons.

For irregular long-crested waves, a high sensitivity in the horizontal response towards wave direction changes of 0.5° and 1.0° is found. Relatively large differences in the rotational response of the bridge is observed, which are partly due to a low accuracy in the measurements. Still, this finding indicates challenges regarding the modelling of the torsional motion of the floating bridge presented in the present paper.

For short-crested waves a low sensitivity towards the main wave direction is found in both the computed and measured response and a good agreement is found using 101 wave directions in the directional spreading function. The same comparison is valid using 51 wave directions but for 11, 12 and 13 wave directions the uncertainty increase.

In the case of adding current to the long-crested waves, an amplifying effect is observed in both the measured and computed response, although the computed response is lower than that of the measured. Due to lack of information, some uncertainty persists regarding whether or not the excitation effect increases with larger significant wave heights and further investigations are needed before any concluding remarks can be made.

Table 8
Standard deviations normalized by H_s. Test 530 and 533 have lower H_s than test 531 and 534. The numerical model is based on $\theta = -89.5°$.

Resp.	Pos.	Unit	Experiment Statens vegvesen (1990)				Numerical			
			U_c = 0.00m/s		U_c = 0.92m/s		U_c = 0.00m/s		U_c = 0.92m/s	
			530	531	533	534	530	531	533	534
Y_G	Pos. 1	[m/m]	3.48e-02	3.62e-02	4.14e-02	4.31e-02	4.78e-02	5.13e-02	4.95e-02	5.48e-02
Y_G	Pos. 2	[m/m]	5.90e-02	6.00e-02	6.65e-02	7.15e-02	7.02e-02	7.52e-02	7.34e-02	8.10e-02
Y_G	Pos. 3	[m/m]	9.92e-02	1.03e-01	1.15e-01	1.26e-01	1.33e-01	1.43e-01	1.38e-01	1.53e-01
Z_G	Pos. 1	[m/m]	2.95e-02	3.31e-02	3.37e-02	3.94e-02	2.20e-02	2.42e-02	2.14e-02	2.38e-02
Z_G	Pos. 2	[m/m]	3.29e-02	3.81e-02	4.05e-02	4.96e-02	3.34e-02	3.71e-02	3.19e-02	3.58e-02
Z_G	Pos. 3	[m/m]	3.89e-02	4.66e-02	4.73e-02	6.05e-02	3.95e-02	4.40e-02	3.75e-02	4.21e-02
R_{X_G}	Pos. 3	[deg/m]	1.81e-01	1.99e-01	1.93e-01	2.05e-01	3.06e-01	3.42e-01	2.87e-01	3.19e-01
M_{Y_G}	Pos. 1	[kNm/m]	7.58e+03	7.31e+03	9.01e+03	7.48e+03	4.99e+03	5.24e+03	5.66e+03	5.81e+03
M_{Z_G}	Pos. 1	[kNm/m]	1.74e+04	1.80e+04	2.00e+04	2.17e+04	2.44e+04	2.63e+04	2.53e+04	2.80e+04
M_{Z_G}	Pos. 3	[kNm/m]	2.87e+04	2.96e+04	3.32e+04	3.62e+04	3.72e+04	3.99e+04	3.86e+04	4.27e+04
Q_{Y_G}	Pos. 1	[kN/m]	3.20e+02	3.27e+02	3.71e+02	3.74e+02	3.72e+02	3.97e+02	3.96e+02	4.33e+02
F_{X_G}	End 1	[kN/m]	1.34e+03	1.44e+03	1.43e+03	1.58e+03	1.56e+03	1.68e+03	1.61e+03	1.76e+03
Q_{Y_G}	End 1	[kN/m]	5.06e+02	5.17e+02	5.84e+02	6.17e+02	5.29e+02	5.66e+02	5.56e+02	6.13e+02
Q_{Z_G}	End 1	[kN/m]	2.18e+02	2.24e+02	2.90e+02	2.58e+02	1.61e+02	1.71e+02	1.66e+02	1.76e+02
M_{X_G}	End 1	[kNm/m]	2.44e+03	2.80e+03	3.37e+03	3.20e+03	2.77e+03	2.81e+03	3.34e+03	3.41e+03

CRediT authorship contribution statement

Thomas Viuff: Conceptualization, Methodology, Investigation, Data curation, Writing - original draft, Formal analysis, Visualization, Validation. **Xu Xiang:** Conceptualization, Methodology, Resources, Writing - review & editing. **Ole Øiseth:** Writing - review & editing. **Bernt Johan Leira:** Supervision, Writing - review & editing.

Declaration of Competing Interest

None.

Acknowledgements

This research was carried out with financial support from the NPRA with funding number 2011067932-58. The authors greatly acknowledge this support and NPRA's permission to publish the experimental data. We would also like to thank our colleagues Dr. Jian Dai and Dr. Ting Liu for their help improving the paper by checking some of the modelling details during the submission phase.

Supplementary material

Supplementary material associated with this article can be found, in the online version, at 10.1016/j.apor.2020.102368.

References

Cummins, W.E., 1962. The Impulse Response Function and Ship Motions. Report no. DTMB-1661. Washington DC, USA.
Delany, N.K., Sorensen, N.E., 1953. Low-Speed Drag of Cylinders of Various Shapes. Technical note 3038. Washington, USA.
DNV, 2010. DNV-RP-C205 Environmental Conditions and Environmental Loads. Oslo, Norway.
DNV, 2014. Wadam - Wave Analysis by Diffraction and Morison Theory, SESAM User Manual. Report no. 94-7100. Høvik, Norway.
Faltinsen, O.M., 1993. Sea Loads on Ships and Offshore Structures. Cambridge University Press.
Goda, Y., 1970. Numerical experiments on wave statistics with spectral simulation. Report Port Harbour Res. Inst. 9, 3–57.
Hasselmann, K., Barnett, T.P., Bouws, E., Carlson, H., Cartwright, D.E., Enke, K., Ewing, J.A., Gienapp, H., Hasselmann, D.E., Kruseman, P., Meerburg, A., Muller, P., Olbers, D.J., Richter, K., Sell, W., Walden, H., 1973. Measurements of wind-wave growth and swell decay during the joint north sea wave project (JONSWAP). Deutsche Hydrographische Zeitschrift 8 (12).
Karimirad, M., Meissonnier, Q., Gao, Z., Moan, T., 2011. Hydroelastic code-to-code comparison for a tension leg spar-type floating wind turbine. Mar. Struct. 24, 412–435. https://doi.org/10.1016/j.marstruc.2011.05.006.
Kvåle, K.A., Øiseth, O., Rønnquist, A., 2017. Operational modal analysis of an end-supported pontoon bridge. Eng. Struct. 148, 410–423. https://doi.org/10.1016/j.engstruct.2017.06.069.
Langen, I., Sigbjörnsson, R., 1980. On stochastic dynamics of floating bridges. Eng. Struct. 2 (4), 209–216. https://doi.org/10.1016/0141-0296(80)90002-4.
Larssen, R.M., Leira, B.J., Remseth, S.N., 1996. Structural parameter identification for marine bridges. Proceedings of the 15th International Conference on Offshore Mechanics and Arctic Engineering. vol. 2. Florence
Løken, A.E., Oftedal, R.A., 1990. Aspects of hydrodynamic loading and response in design of floating bridges. Second Symp. Strait Crossings 479–486.
Næser, H., 1981. NHL - Ocean basin capabilities and limitations. Proceedings of the International Symposium on Hydrodynamics in Ocean Engineering, Trondheim. The Norwegian Institute of Technology, pp. 1191–1210.
Petersen, Ø.W., Øiseth, O., 2017. Sensitivity-based finite element model updating of a pontoon bridge. Eng. Struct. 150, 573–584. https://doi.org/10.1016/j.engstruct.2017.07.025.
Robertson, A., Jonkman, J., Vorpahl, F., Popko, W., Qvist, J., Frøyd, L., Chen, X., Azcona, J., Uzunoglu, E., Soares, C.G., Luan, C., Yutong, H., Pengcheng, F., Yde, A., Larsen, T., Nichols, J., Buils, R., Lei, L., Nygaard, T.A., Manolas, D., Heege, A., Vatne, S.R., Ormberg, H., Duarte, T., Godreau, C., Hansen, H.F., Nielsen, A.W., Riber, H., Cunff, C.L., Beyer, F., Yamaguchi, A., Jung, K.J., Shin, H., Shi, W., Park, H., Alves, M., Gurinel, M., 2014. Offshore code comparison collaboration continuation within IEA wind task 30: phase ii results regarding a floating semisubmersible wind system. Proceedings of the 33rd International Conference on Ocean, Offshore and Arctic Engineering. ASMEhttps://doi.org/10.1115/OMAE2014-24040.
Shao, Y., Xiang, X., Liu, J., 2019. Numerical investigation of wave-frequency pontoon responses of a floating bridge based on model test results. Proceedings of the 38th International Conference on Offshore Mechanics and Arctic Engineering.
SINTEF Ocean, 2018a. RIFLEX 4.14.0 Theory Manual. Trondheim, Norway.
SINTEF Ocean, 2018b. SIMO 4.14.0 Theory Manual. Trondheim, Norway.
Sørum, S.H., Horn, J.-T.H., Amdahl, J., 2017. Comparison of numerical response predictions for a bottom-fixed offshore wind turbine. Energy Procedia 137, 89–99. https://doi.org/10.1016/j.egypro.2017.10.336.
Statens vegvesen, 1989. Modellforsøk med Flytebru: Kontinuerlig Pontongbru. Report no. MT40 F89-0252. Oslo, Norway.
Statens vegvesen, 1990. Sammenligning mellom modellforsøk og beregninger av en enkelt pongtong og en flytebru med separate pongtonger. Report no. 89-3440. Høvik, Norway.
Villoria, B., 2016. Floating bridge technology - prediction of extreme environmental load effects. Proceedings of the 35th International Conference on Ocean, Offshore and Arctic Engineering. ASME, pp. 1–8. https://doi.org/10.1115/OMAE2016-54433.
Viuff, T., Leira, B.J., Xiang, X., Øiseth, O., 2019. Effects of wave directionality on extreme response for a long end-anchored floating bridge. Appl. Ocean Res. 90, 101843. https://doi.org/10.1016/j.apor.2019.05.028.
Viuff, T., Xiang, X., Leira, B.J., Øiseth, O., 2020. Software-to-software comparison of end-anchored floating bridge global analysis. Journal of Bridge Engineering. In Print
Xiang, X., Løken, A., 2019. Hydroelastic analysis and validation of an end-anchored floating bridge under wave and current loads. Proceedings of the 38th International Conference on Offshore Mechanics and Arctic Engineering. pp. 1–9.
Zhao, R., Faltinsen, O.M., Krokstad, J.R., Aanesland, V., 1988. Wave-current interaction effects on large-volume structures. Proc. Int. Conf. Behaviour of Offshore Structures. 2. pp. 623–638.